The Astrophysical Journal, 883:178 (9pp), 2019 October 1 https://doi.org/10.3847/1538-4357/ab3e01
© 2019. The American Astronomical Society. All rights reserved.

Turbulence versus Fire-hose Instabilities: 3D Hybrid Expanding Box Simulations

Petr Hellinger[1,2], Lorenzo Matteini[3], Simone Landi[4,5], Luca Franci[6], Andrea Verdini[4], and Emanuele Papini[4]
[1] Astronomical Institute, CAS, Bocni II/1401, Prague CZ-14100, Czech Republic; petr.hellinger@asu.cas.cz
[2] Institute of Atmospheric Physics, CAS, Bocni II/1401, Prague CZ-14100, Czech Republic
[3] LESIA, Observatoire de Paris, Université PSL, CNRS, Sorbonne Université, Univ. Paris Diderot, Sorbonne Paris Cité, place Jules Janssen 5, F-92195 Meudon, France
[4] Dipartimento di Fisica e Astronomia, Università degli Studi di Firenze, via G. Sansone 1, Sesto Fiorentino I-50019, Italy
[5] INAF, Osservatorio Astrofisico di Arcetri, Largo E. Fermi 5, Firenze I-50125, Italy
[6] School of Physics and Astronomy, Queen Mary University of London, London E1 4NS, UK
Received 2019 April 30; revised 2019 August 21; accepted 2019 August 21; published 2019 October 3

Abstract

The relationship between a decaying plasma turbulence and proton fire hose instabilities in a slowly expanding plasma is investigated using three-dimensional hybrid expanding box simulations. We impose an initial ambient magnetic field along the radial direction, and we start with an isotropic spectrum of large-scale, linearly polarized, random-phase Alfvénic fluctuations with zero cross-helicity. A turbulent cascade rapidly develops and leads to a weak proton heating that is not sufficient to overcome the expansion-driven perpendicular cooling. The plasma system eventually drives the parallel and oblique fire hose instabilities that generate quasi-monochromatic wave packets that reduce the proton temperature anisotropy. The fire hose wave activity has a low amplitude with wave vectors quasi-parallel/oblique with respect to the ambient magnetic field outside of the region dominated by the turbulent cascade and is discernible in one-dimensional power spectra taken only in the direction quasi-parallel/oblique with respect to the ambient magnetic field; at quasi-perpendicular angles the wave activity is hidden by the turbulent background. These waves are partly reabsorbed by protons and partly couple to and participate in the turbulent cascade. Their presence reduces kurtosis, a measure of intermittency, and the Shannon entropy, but increases the Jensen–Shannon complexity of magnetic fluctuations; these changes are weak and anisotropic with respect to the ambient magnetic field and it is not clear if they can be used to indirectly discern the presence of instability-driven waves.

Key words: instabilities – turbulence

1. Introduction

The solar wind is a turbulent flow of weakly collisional plasma and constitutes a natural laboratory for plasma turbulence (Alexandrova et al. 2013; Bruno & Carbone 2013). Properties of plasma turbulence and its dynamics remain an open challenging problem (Petrosyan et al. 2010; Matthaeus & Velli 2011). At large scales it can be described by the magnetohydrodynamic (MHD) approximation, accounting for the dominant nonlinear coupling and for the presence of the ambient magnetic field that introduces a preferred direction (Shebalin et al. 1983; Oughton et al. 1994; Verdini et al. 2015). Around particle characteristic scales the plasma description has to be extended beyond MHD (see Papini et al. 2019, and references therein) and a transfer of the cascading energy to particles is expected. Observed radial profiles of proton temperatures indicate an important heating that is often comparable to the estimated turbulent energy cascade rate (MacBride et al. 2008; Cranmer et al. 2009; Hellinger et al. 2013). Alpha particles also need to be heated (Stansby et al. 2019), whereas for electrons it is much less clear because of their strong heat flux (Štverák et al. 2015).

The nonlinearly coupled turbulent system is also characterized by non-Gaussian statistical properties, a phenomenon called intermittency. For a given quantity Y (e.g., a component of the magnetic field, bulk velocity field) and a separation length l, the increment, ΔY, the difference between two points separated by l, generally has a non-Gaussian distribution. This non-Gaussianity is well characterized by the excess kurtosis (flatness) that is close to zero on large scales (compatible with a Gaussian statistics) but it increases as l decreases in the inertial ranges; behavior of the kurtosis in the sub-ion range is not well known, some results indicate that it further increases (e.g., Alexandrova et al. 2008; Franci et al. 2015) but some observations and numerical simulations indicate that the kurtosis saturates and even decreases in the sub-ion range (e.g., Wu et al. 2013; Parashar 2018). The non-Gaussian statistics with extreme values is often associated with localized/coherent structures that appear to be important for the particle energization (Matthaeus et al. 2015); these energization/dissipation processes could be responsible for the decrease of the kurtosis.

Recently, the Shannon entropy, H, and the Jensen–Shannon complexity, C (see below for definitions), two related quantities that measure the information content in time series and allow us to discern chaotic versus stochastic behavior (Maggs & Morales 2013), were used to characterize turbulent fluctuations observed in situ or in laboratory plasmas (Weck et al. 2015). The time series of the solar wind magnetic field exhibit a relatively large normalized permutation (Shannon) entropy ($H \gtrsim 0.9$), and a small statistical (Jensen–Shannon) complexity ($C \lesssim 0.15$) (Weck et al. 2015; Olivier et al. 2019; Weygand & Kivelson 2019). In situ observations also indicate that during the radial evolution the permutation entropy H increases, whereas the complexity C decreases and these statistical parameters in the (H, C) plane have properties similar to those predicted for a fractional Brownian motion (Weygand & Kivelson 2019); interestingly, the fractional Brownian motion may be regarded as a natural boundary between chaotic and stochastic processes (Maggs & Morales 2013); however, the

connection between these two statistical parameters and properties of the solar wind turbulence is unclear.

The radial expansion further complicates the evolution of the solar wind turbulence. It induces an additional damping, turbulent fluctuations decrease due to the expansion (as well as due to the turbulent decay) slowing down the turbulent cascade (see Grappin et al. 1993; Dong et al. 2014). Furthermore, the expansion also introduces another preferred direction (the radial one; Verdini & Grappin 2015) and the characteristic particle scales change with radial distance. The understanding of the complex nonlinear properties of plasma turbulence on particle scales is facilitated via a numerical approach (Servidio et al. 2015; Franci et al. 2018b). Direct kinetic simulations of turbulence show that particles are indeed on average heated by the cascade (Parashar et al. 2009; Markovskii & Vasquez 2011; Wu et al. 2013; Franci et al. 2015; Arzamasskiy et al. 2019); moreover, turbulence leads locally to complex anisotropic and nongyrotropic distribution functions (Valentini et al. 2014; Servidio et al. 2015). On the other hand, the solar wind expansion naturally generates particle temperature anisotropies (Matteini et al. 2007, 2012). The anisotropic and nongyrotropic features may be a source of free energy for kinetic instabilities. There are indications that such instabilities are active in the solar wind. Apparent bounds on ion parameters are observed that are relatively in agreement with theoretical kinetic linear predictions (Gary et al. 2001; Hellinger et al. 2006; Maruca et al. 2012; Matteini et al. 2013; Klein et al. 2018). Furthermore, wave activity driven by the kinetic instabilities associated with the ion temperature anisotropies and/or differential velocity is often observed (Jian et al. 2009; Gary et al. 2016; Wicks et al. 2016). This activity is usually in the form of a narrowband enhancement of the magnetic power spectral density at ion scales "on top of" the background turbulent magnetic field; these fluctuations tend to be relatively coherent (Lion et al. 2016).

Hellinger et al. (2015) used a two-dimensional (2D) hybrid expanding box (HEB) model to study the relationship between the proton oblique fire hose instability and plasma turbulence. They showed that the instability and plasma turbulence can coexist and that the instability bounds the proton temperature anisotropy in an inhomogeneous/nonuniform turbulent system. The results of Hellinger et al. (2015) are, however, strongly constrained by the 2D geometry with the ambient magnetic field being perpendicular to the simulation plane and one expects that unstable modes appear at quasi-parallel/oblique angles with respect to the background magnetic field based on the linear (uniform and homogeneous) theory (see Gary 1993; Klein & Howes 2015). In this paper we extend the work of Hellinger et al. (2015) using a three-dimensional (3D) version of the HEB model. We investigate the real-space and spectral properties of turbulent fluctuations and the impact of fire hose-driven waves. We also analyze the effects of this wave activity on the statistical properties (intermittency, permutation entropy, complexity) of turbulence and test if these quantities could be used as a mean to discern the presence of the fire-hose waves.

2. Numerical Code

In this paper we use a 3D version of the HEB model implemented in the numerical code CAMELIA (Franci et al. 2018a) that allows us to study self-consistently different physical processes at ion scales (see Ofman 2019). The expanding box uses coordinates comoving with the solar wind plasma, assuming a constant solar wind radial velocity v_{sw}, and approximating the spherical coordinates by the Cartesian ones (Hellinger & Trávníček 2005). The radial distance R of the box follows $R = R_0(1 + t/t_{exp})$, where R_0 is the initial position and $t_{exp} = R_0/v_{sw}$ is the (initial) characteristic expansion time. Transverse scales of the simulation box (with respect to the radial direction) increase $\propto R$, whereas the radial scale remains constant. The model uses the hybrid approximation where electrons are considered a massless, charge-neutralizing fluid, and ions are described by a particle-in-cell model (Matthews 1994). Fields and moments are defined on a 3D grid $512 \times 512 \times 256$; periodic boundary conditions are assumed. The initial spatial resolution is $\Delta x = \Delta y = 0.25 d_i$, $\Delta z = 0.5 d_i$, where $d_i = v_A/\omega_{ci}$ is the initial proton inertial length (v_A is the initial Alfvén velocity, and ω_{ci} is the initial proton gyrofrequency). There are 400 macroparticles per cell for protons, which are advanced with a time step $\Delta t = 0.05/\omega_{ci}$, while the magnetic field is advanced with a smaller time step, $\Delta t_B = \Delta t/10$. The initial ambient magnetic field is directed along the z (radial) direction, $\boldsymbol{B}_0 = (0, 0, B_0)$, and we impose a continuous expansion in the x and y directions with the initial expansion time $t_{exp} = 10^4 \omega_{ci}^{-1}$. Due to the expansion with the strictly radial magnetic field the ambient density and the magnitude of the ambient magnetic field decrease as $\langle n \rangle \propto \langle B \rangle \propto R^{-2}$ (the proton inertial length d_i increases $\propto R$, the ratio between the transverse sizes and d_i remains constant, and the ratio between the radial size and d_i decreases as R^{-1}).

We initially set the parallel proton beta $\beta_\parallel = 2.4$ and the proton temperature anisotropy $T_\perp/T_\parallel = 0.75$; for these parameters the plasma system is stable with respect to the fire hose instabilities. Electrons are assumed to be isotropic and isothermal with $\beta_e = 1$. We initialize the simulation with an isotropic 3D spectrum of modes with random phases, linear Alfvén polarization ($\delta\boldsymbol{B} \perp \boldsymbol{B}_0$), and vanishing correlation between magnetic and velocity fluctuations (zero cross-helicity). These modes are in the range $0.02 \leqslant k d_i \leqslant 0.2$ and have a flat one-dimensional (1D; omnidirectional) power spectrum with rms fluctuations $=0.24 B_0$. A small resistivity η is used to avoid accumulation of cascading energy at grid scales; we set $\eta = 0.001 \mu_0 v_A^2/\omega_{ci}$ (μ_0 being the magnetic permittivity of vacuum).

3. Simulation Results

3.1. Global Evolution

The evolution of the system is shown in Figure 1, which displays quantities averaged over the simulation box: the (rms) total fluctuating magnetic field δB and the fluctuating magnetic field δB_l with large parallel wave vectors (i.e., for for $|k_\parallel| d_i > 0.25$), the mean square of the electric current, $|\boldsymbol{J}|^2$, the mean proton temperature anisotropy $T_\perp/T_\parallel$, and the mean proton agyrotropy $A_\varnothing$ as functions of time. The agyrotropy $A_\varnothing$ is defined here following Scudder & Daughton (2008) as

$$A_\varnothing = 2\frac{|P_{\perp 1} - P_{\perp 2}|}{P_{\perp 1} + P_{\perp 2}}, \quad (1)$$

where $P_{\perp 1}$ and $P_{\perp 2}$ are the are the two eigenvalue components of the (proton) pressure tensor perpendicular to the local magnetic field.

The level of total magnetic fluctuations, δB initially shortly increases as the turbulent cascade develops and a part of the kinetic proton energy is transformed to the magnetic one (see

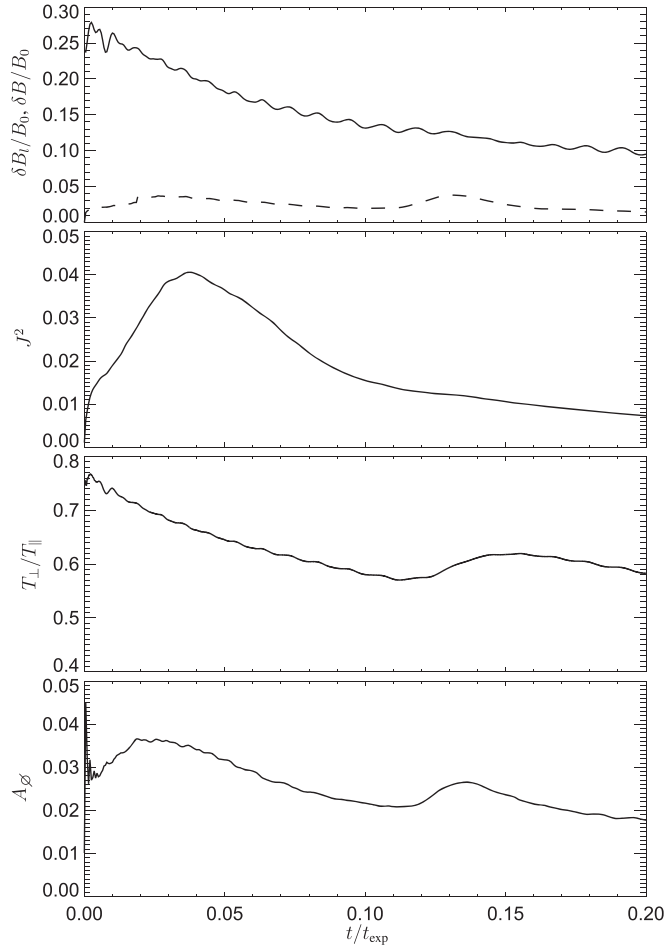


Figure 1. Evolution of (from top to bottom) the total fluctuating magnetic field, δB (solid line), and the fluctuating magnetic field with large parallel wave vectors, δB_l (dashed line), the mean square of the electric current $|\boldsymbol{J}|^2$, the mean proton temperature anisotropy $T_\perp/T_\parallel$, and the mean proton agyrotropy $A_\varnothing$ as functions of time.

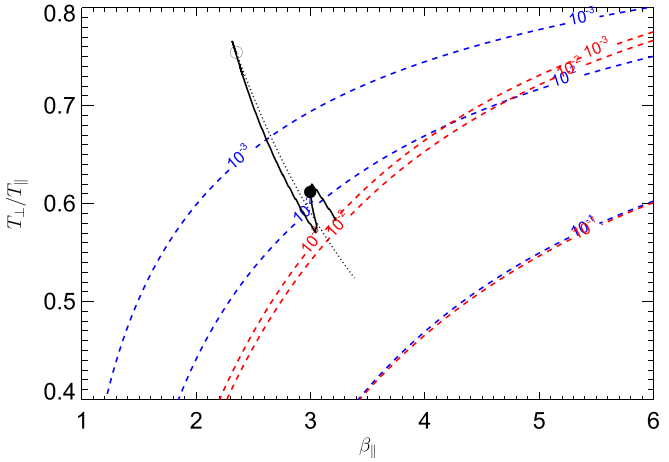


Figure 2. Evolution of the system in ($\beta_\parallel$, $T_\perp/T_\parallel$) space (solid line). The empty circle denotes the initial condition, whereas the full circle denotes the time $t = 0.14t_{\rm exp}$; the dotted line shows the double-adiabatic prediction for a corresponding system without turbulent fluctuations. The blue and red dashed contours show the maximum growth rate (normalized to ω_{ci}) of the parallel and oblique fire-hose instability (for a uniform and homogeneous bi-Maxwellian system), respectively.

Franci et al. 2015). After that short transient period, δB overall decreases and oscillates with a small amplitude due to the superposition of large-scale propagating Alfvén modes. The amplitude of magnetic fluctuations with $|k_\parallel| d_i > 0.25$, δB_l (top panel of Figure 1, dashed line), initially increases and reaches a local maximum around $t = 0.025t_{\rm exp}$ as the turbulent cascade develops. After that it decreases until it reaches another local maximum at about $t = 0.13t_{\rm exp}$. The mean amplitude of the current, $|\boldsymbol{J}|$, initially increases and reaches a maximum at about $t = 0.04t_{\rm exp}$, which indicates the presence of a well-developed turbulent cascade (Mininni & Pouquet 2009; Valentini et al. 2014). After that, $|\boldsymbol{J}|$ decreases with a hint of a slower decrease rate around $t = 0.13t_{\rm exp}$. The temperature anisotropy, $T_\perp/T_\parallel$, after an initial transition decreases (with weak oscillations), but it increases from $t \sim 0.12t_{\rm exp}$ to $\sim 0.15t_{\rm exp}$ (and the system becomes less anisotropic), when modes with large parallel wave vectors appear; after $t \sim 0.16t_{\rm exp}$, $T_\perp/T_\parallel$ decreases again. The agyrotropy, $A_\varnothing$, starts from the initial noise level 0.01, strongly varies during the short relaxation of the initial conditions and then increases, reaches a maximum at around $t = 0.02t_{\rm exp}$ and decreases. Later on, at the same time the proton anisotropy is reduced, the agyrotropy increases again, reaches a maximum around $0.14t_{\rm exp}$, then decreases. The turbulent cascade creates velocity shears at ion scales that naturally generate anisotropy as well as agyrotropy (Del Sarto & Pegoraro 2018). Figure 1 suggests that the reduction of the temperature anisotropy occurring at $t \sim 0.12t_{\rm exp} - 0.15t_{\rm exp}$ is related to the development of fire hose-like instabilities generating fluctuations with large parallel wave vectors. While the fire hose instability-driven fluctuations reduce their source of free energy, they enhance the agyrotropy.

Figure 2 shows the evolution of the system in ($\beta_\parallel$, $T_\perp/T_\parallel$) space that is useful to parameterize the linear stability of a (uniform and homogeneous) plasma with respect to temperature anisotropy-driven instabilities (Gary et al. 2001). Figure 2 shows that after the initial transient evolution, $T_\perp/T_\parallel$ decreases and $\beta_\parallel$ increases somewhat similarly to the double-adiabatic prediction ($T_\perp \propto R^{-2}$, $T_\parallel = $ const.). During this phase, $\beta_\parallel$ increases whereas $T_\perp/T_\parallel$ decreases. Eventually, the system reaches parameters that are unstable (with respect to the parallel fire hose) in the corresponding uniform and homogeneous plasma. Before reaching the region unstable with respect to the oblique fire-hose instability the system moves toward the stable region and $T_\perp/T_\parallel$ increases, whereas $\beta_\parallel$ decreases. This reduction of the proton anisotropy stops after some time and $T_\perp/T_\parallel$ decreases and $\beta_\parallel$ increases until the end of the simulation. The last part of the path of the system in the ($\beta_\parallel$, $T_\perp/T_\parallel$) space is very similar to results from HEB simulations without turbulent fluctuations (see Hellinger 2017) when the system is under the influence of the parallel and oblique fire-hose instabilities. The latter is particularly efficient in reducing the proton temperature anisotropy due to its peculiar nonlinear evolution: the oblique fire hose generates non-propagating modes that only exist for a sufficiently strong proton parallel temperature anisotropy. As these modes grow they scatter protons and reduce their temperature anisotropy. Consequently, they destroy the non-propagating branch and transform (via the linear mode conversion) to propagating modes that are damped and during this process they further reduce the temperature anisotropy (Hellinger & Matsumoto 2000, 2001). We observe a similar evolution in the present simulation.

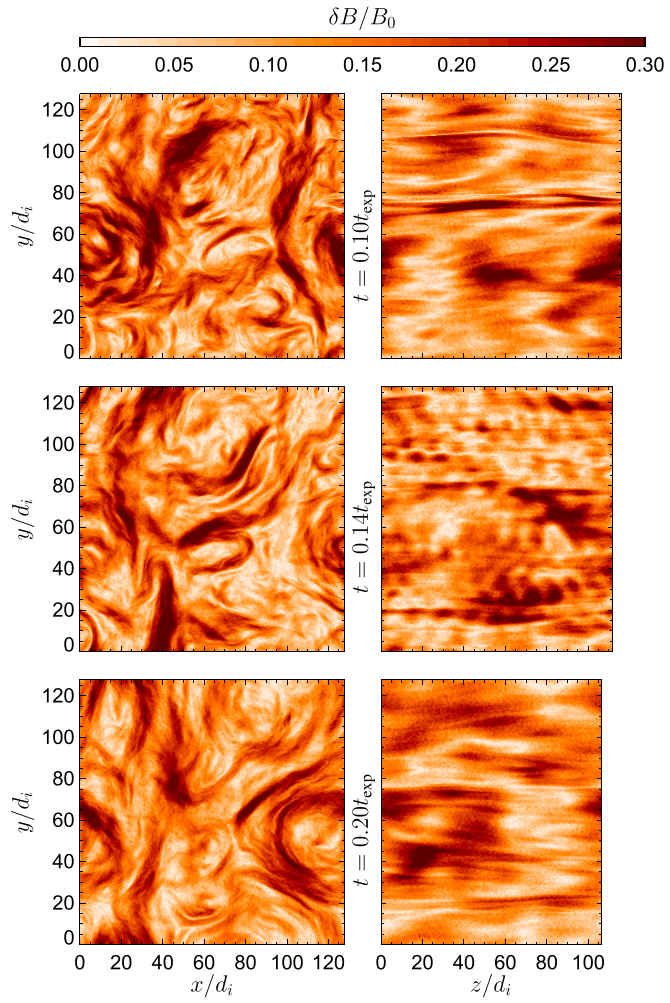


Figure 3. Color-scale plots of 2D cuts of δB (normalized to B_0) as functions of (x, y) (left) and (z, y) (right) for $t = 0.10t_{exp}$ (top), $t = 0.14t_{exp}$ (middle), and $t = 0.20t_{exp}$ (bottom).

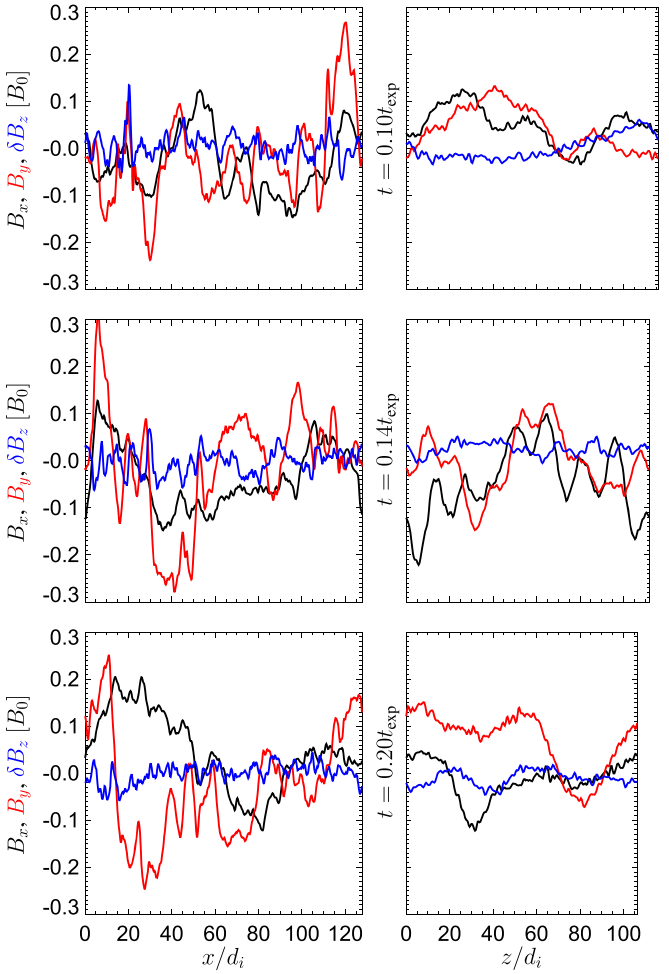


Figure 4. 1D cuts of the fluctuating magnetic field components (black) B_x, (red) B_y, and (blue) δB_z (normalized to B_0) as functions of x (and $y = z = 0$, left) and z (and $x = y = 0$, right) for $t = 0.10t_{exp}$ (top), $t = 0.14t_{exp}$ (middle), and $t = 0.20t_{exp}$ (bottom).

3.2. Physical Space

We will now look at the properties of the simulated system at three different times, at $t = 0.10t_{exp}$, before the onset of the fire-hose instabilities, at $t = 0.14t_{exp}$ around the maximum activity of the instabilities, and at the end, $t = 0.20t_{exp}$. Figure 3 shows the real-space structure of the magnetic fluctuations at the three times. It shows 2D cuts of δB as functions of (x, y) and (z, y). At $t = 0.10t_{exp}$ Figure 3 (top panels) shows a developed turbulence with complex anisotropic properties. In the (x, y) cut there are signatures of nonlinear structures (such as current sheets and magnetic islands), whereas the (z, y) cut also exhibits large-scale wavy behavior (see Franci et al. 2018b). At $t = 0.14t_{exp}$ (Figure 3, middle panels) the (x, y) cut remains qualitatively the same as that at $t = 0.10t_{exp}$, but in the (z, y) cut there is clear wave activity, in the form of localized quasi-coherent wave packets (with wavelengths of the order of $10d_i$), on top of the turbulent background. At the end, $t = 0.20t_{exp}$, the (x, y) cut is still qualitatively unchanged and the (z, y) cut is similar to that at $t = 0.10t_{exp}$. Note that a similar real-space structure is also observed for other quantities (e.g., ion bulk velocity, density, currents, temperature anisotropy/agyrotropy); all these quantities are more uniform along the ambient magnetic field or rather along the magnetic field lines.

To approach in situ 1D observations we investigate 1D spatial cuts through the simulation box for the three times. Figure 4 shows 1D plots of the fluctuating magnetic field components B_x, B_y, and δB_z normalized to B_0 as functions of x (and $y = z = 0$, left) and z (and $x = y = 0$, right). As in Figure 3 the perpendicular cuts (Figure 4, left panels) are strongly structured but it is hard to discern any similarities between the three times (except perhaps qualitative ones). In the parallel cuts there are mostly large-scale fluctuations at $t = 0.10t_{exp}$ and $t = 0.20t_{exp}$. At $t = 0.14t_{exp}$ there are, on top of the large-scale turbulent fluctuations, shorter-wavelength wave packets owing to the fire-hose instabilities. Figure 4 also shows that the compressible component δB_z is weak with respect to B_x and B_y for the turbulent as well as the fire-hose fluctuations. Note that the radial (z) size of the simulation box normalized to the proton inertial length decreases with time.

3.3. Spectral Properties

Let us now investigate the spectral properties of the fluctuations shown in Figure 3. Figure 5 shows the 2D power spectral densities (PSDs) of the magnetic field, $\boldsymbol{B}$, and the ion bulk velocity, $\boldsymbol{u}$, as functions of $k_\perp$ and $k_\parallel$ at the three times. At $t = 0.10t_{exp}$, Figure 5 (top panels) demonstrates that the initial isotropic spectrum develops into a strongly anisotropic

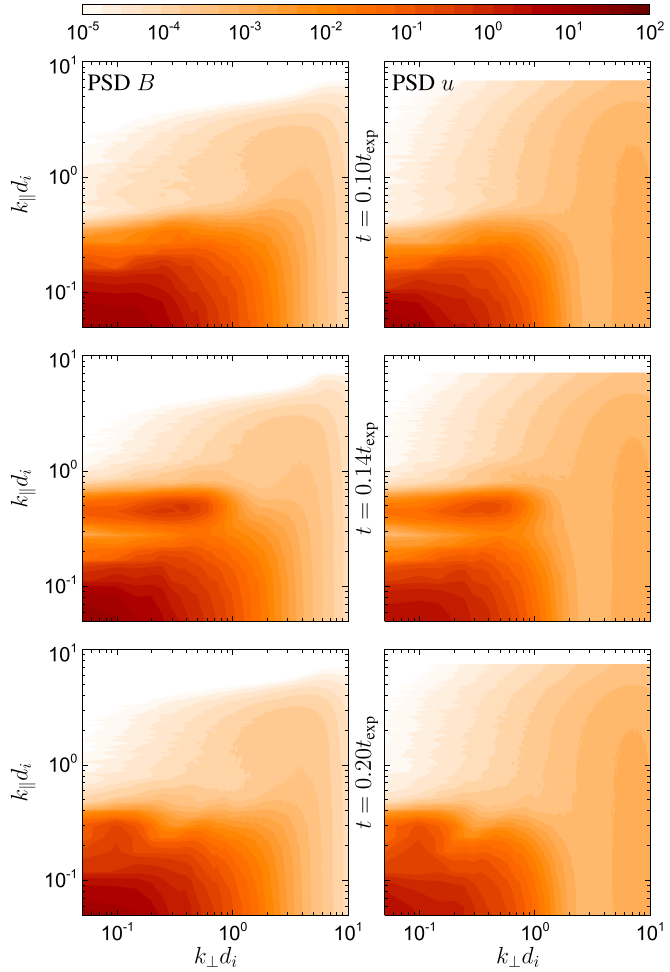


Figure 5. Color-scale plots of the power spectral densities of the magnetic field $\boldsymbol{B}$ (left) and the proton bulk velocity field $\boldsymbol{u}$ (right) as functions of $k_\perp$ and $k_\parallel$ for $t = 0.10t_{exp}$ (top), $t = 0.14t_{exp}$ (middle), and $t = 0.20t_{exp}$ (bottom).

spectrum with a cascade preferably at strongly oblique angles with respect to the ambient magnetic field (see Franci et al. 2018b). At $t = 0.14t_{exp}$ (Figure 5, middle panels) there is a similar turbulent spectrum; moreover, there is a narrow band in $k_\parallel$ (at $k_\parallel \sim 0.5/d_i$) enhancement at quasi-parallel/oblique angles with respect to the background magnetic field. At $t = 0.20t_{exp}$ this narrowband enhancement is not clearly discernible but there are some indications that some of the fluctuating energy remained (around $k_\perp \sim 0.1/d_i$ and $k_\parallel \sim 0.2/d_i$).

It is interesting to look at the reduced 1D power spectra, as these correspond to what is usually obtained from observational spacecraft data. Figure 6 shows a comparison between the reduced parallel and perpendicular 1D PSDs of $\boldsymbol{B}$ and $\boldsymbol{u}$ at the same three times as in Figure 3. In the perpendicular direction, the PSDs of $\boldsymbol{B}$ and $\boldsymbol{u}$ as functions of $k_\perp$ (Figure 6, left panels) show a little variation between the three times. The fire-hose wave activity is not discernible here. The PSDs of B and u exhibit a steepening at ion scales and some noise at smaller scales (numerical noise is especially visible in the velocity fluctuations due to the limited number of particles per cell). On the other hand, in the parallel direction, the PSDs of $\boldsymbol{B}$ and $\boldsymbol{u}$ as functions of $k_\parallel$ (Figure 6, right panels) exhibit a clear narrow peak at $t = 0.14t_{exp}$ (dashed line) compared to both $t = 0.10t_{exp}$

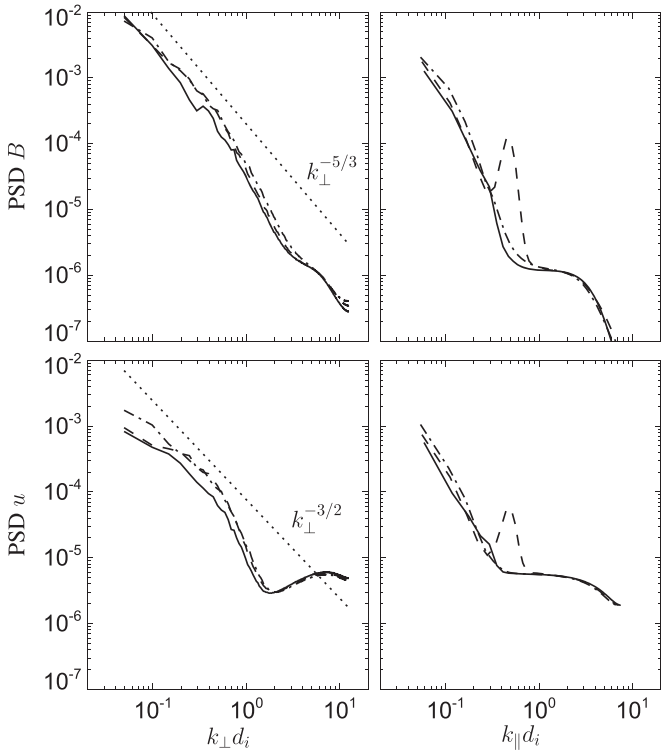


Figure 6. Reduced 1D power spectral densities of (top) $\boldsymbol{B}$ and (bottom) $\boldsymbol{u}$ as functions of (left) $k_\perp$ and (right) $k_\parallel$ for (dashed–dotted) $t = 0.10t_{exp}$, (dashed) $t = 0.14t_{exp}$, and (solid) $t = 0.20t_{exp}$. The dotted lines show (top left) a Kolmogorov-like spectrum $\propto k_\perp^{-5/3}$ and (bottom left) a spectrum $\propto k_\perp^{-3/2}$.

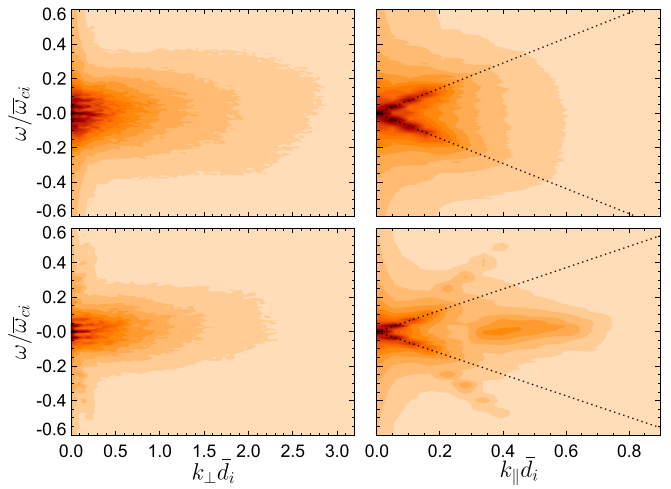


Figure 7. Spatiotemporal spectral properties of magnetic fluctuations: reduced 2D spectra of $\boldsymbol{B}$ as functions of (left) $k_\perp$ and ω and (right) $k_\parallel$ and ω for (top) $t = 0 \div 0.1t_{exp}$ and (bottom) $t = 0.1 \div 0.2t_{exp}$. The wave vectors are normalized to the mean (over the given time interval) inertial length $\bar{d}_i$ and the frequency is normalized to the mean cyclotron frequency $\overline{\omega}_{ci}$. The dotted lines denote the dispersion relation of Alfvén waves.

and $t = 0.20t_{exp}$. Also, here the small-scale fluctuations are dominated by numerical noise.

Further analysis shows that only for angles between the ambient magnetic field and the wave vector below $\sim 40^o$ are the fire-hose fluctuations discernible in the corresponding reduced 1D power spectra.

Figure 7 shows the reduced parallel and perpendicular 2D spatio-temporal spectra of magnetic fluctuations during two phases, $t = 0 \div 0.1t_{exp}$ and $t = 0.1 \div 0.2t_{exp}$. During the first

phase, the turbulent-only phase, the perpendicular spectrum $\delta B(k_\perp, \omega)$ is broadly distributed around the zero frequency; the spread is very large for $k_\perp$ close to 0. During the second phase, the fire-hose phase, the perpendicular spectrum is similar but somewhat weaker. The behavior of the parallel spectrum $\delta B(k_\parallel, \omega)$ is different. During the first phase the spectrum (for small $k_\parallel$) clearly exhibits Alfvénic dispersion: $\omega = \pm k_\parallel \bar{v}_A$ (shown by the dotted lines), where $\bar{v}_A$ is the mean (over the given time interval) Alfvén velocity including the effects of the proton temperature anisotropy. During the second phase, these Alfvénic fluctuations are reduced and the parallel spectrum contains fast-magnetosonic dispersive modes ($\omega \propto \pm k_\parallel^2$) for $0.2 \lesssim k_\parallel \lesssim 0.4$ and weakly or non-propagating modes at $0.3 \lesssim k_\parallel \lesssim 0.6$. The former modes are likely due to the parallel fire hose (Gary et al. 1998; Matteini et al. 2006), whereas the latter are likely related to the oblique fire hose (Hellinger & Trávníček 2008).

3.4. Velocity Distribution Function

The analysis above indicates that the expansion drives the system unstable with respect to the parallel and oblique fire-hose instabilities despite the presence of a developed anisotropic turbulent cascade. The fire-hose wave activity appears at quasi-parallel/oblique angles with respect to the background magnetic field, outside the region in $(k_\perp, k_\parallel)$ where the turbulent fluctuations dominate. The generated wave activity is likely partly damped (as expected for the oblique fire hose) and partly blends into the turbulent fluctuations. Figure 8 shows the gyro-averaged proton velocity distribution function at different times. This figure shows that at $t = 0.10t_e$ the function is deformed with respect to the initial bi-Maxwellian distribution function due to the turbulent heating (see Arzamasskiy et al. 2019); at $v_\parallel \sim 3v_A$ there are signatures of the cyclotron heating owing to the Alfvén (cyclotron) waves. At $t = 0.14t_e$ the proton velocity distribution function exhibits strong wings due to the standard and anomalous cyclotron resonance between the protons and fire-hose waves. The signature of this interaction is weakened at $t = 0.20t_e$ but still discernible.

3.5. Statistical Properties

It is interesting to look at how the fire-hose wave activity affects the statistical properties of turbulence. The turbulent cascade leads to a non-Gaussian character of the fluctuations, i.e., intermittency, which is likely affected by the wave activity generated by the fire-hose instabilities. We calculated the excess kurtosis $K' = K - 3$ in the separation space $(l_\perp, l_\parallel)$ over the simulation box for the increment $\delta B_y = B_y(x + l_\perp, y, z + l_\parallel) - B_y(x, y, z)$. The maximum value of K' appears at $l_\parallel = 0$ and evolves with the time: it initially reaches values of the order of 10 and after $t \simeq 0.05t_{\rm exp}$ it stays at about 3 and slowly decreases; there is no discernible effect of the fire hose instabilities on it. K' is, however, very anisotropic. Figure 9 shows K' as a function of $l_\perp$ and $l_\parallel$ at the three times $t = 0.10t_{\rm exp}$ $t = 0.14t_{\rm exp}$, and $t = 0.20t_{\rm exp}$. The kurtosis is similar at $t = 0.10t_{\rm exp}$ and $t = 0.20t_{\rm exp}$ (at the latter time is somewhat weaker): it is strongly dependent on $l_\perp$, increases as $l_\perp$ decreases but when approaching the spatial resolutions K' saturates and decreases. At $t = 0.14t_{\rm exp}$ the kurtosis is noticeably reduced at the quasi-parallel direction, likely owing to the presence of quasi-parallel/oblique waves.

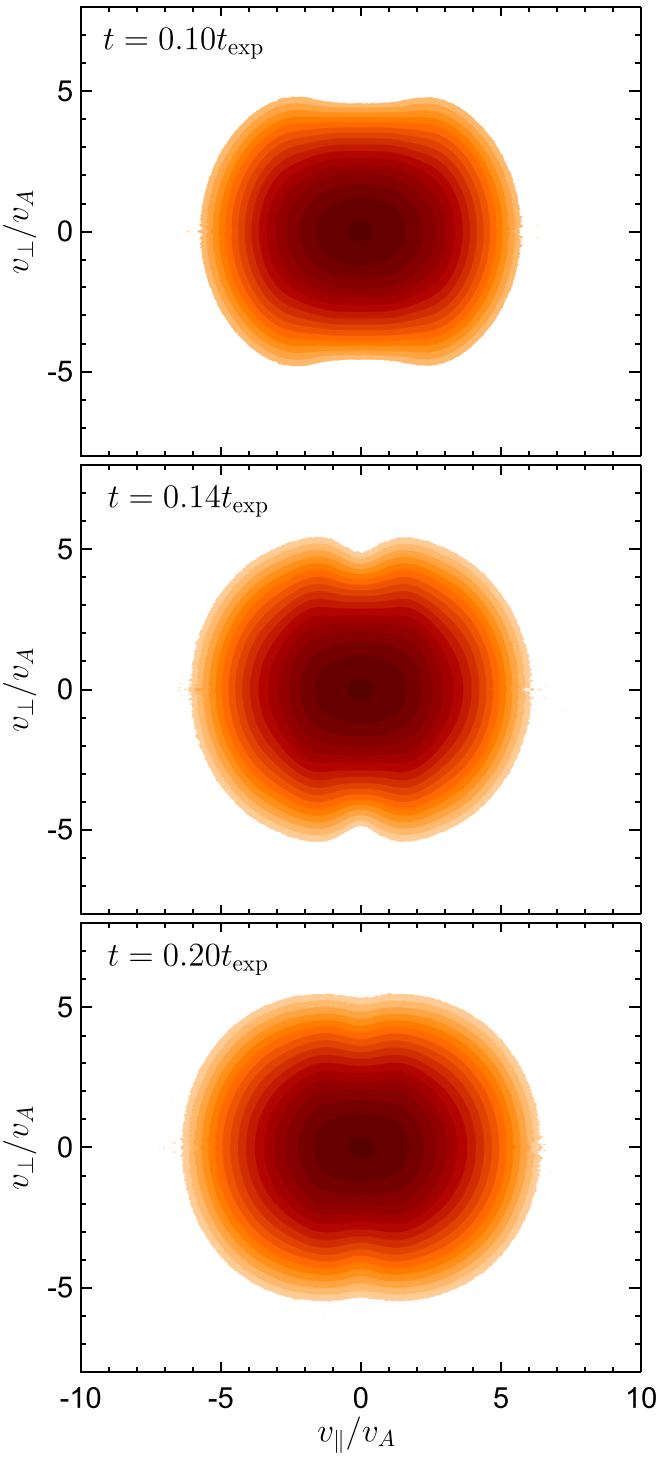


Figure 8. Gyro-averaged proton velocity distribution function f as a function of parallel and perpendicular velocities $v_\parallel$ and $v_\perp$ (with respect to the background magnetic field) for (top) $t = 0.10t_e$, (middle) $t = 0.14t_e$, and (bottom) $t = 0.20t_e$.

Finally, it is interesting to look at how the fire-hose wave activity affects the permutation entropy H and the Jensen–Shannon complexity C (López-Ruiz et al. 1995; Bandt & Pompe 2002; Lamberti et al. 2004). The (normalized) permutation entropy is defined for a time series where for n consecutive points one calculates the probability for each permutation of larger/smaller ordering p_j. For this probability vector $\boldsymbol{p} = \{p_j\}_{j=1,n!}$ the information/Shannon entropy is

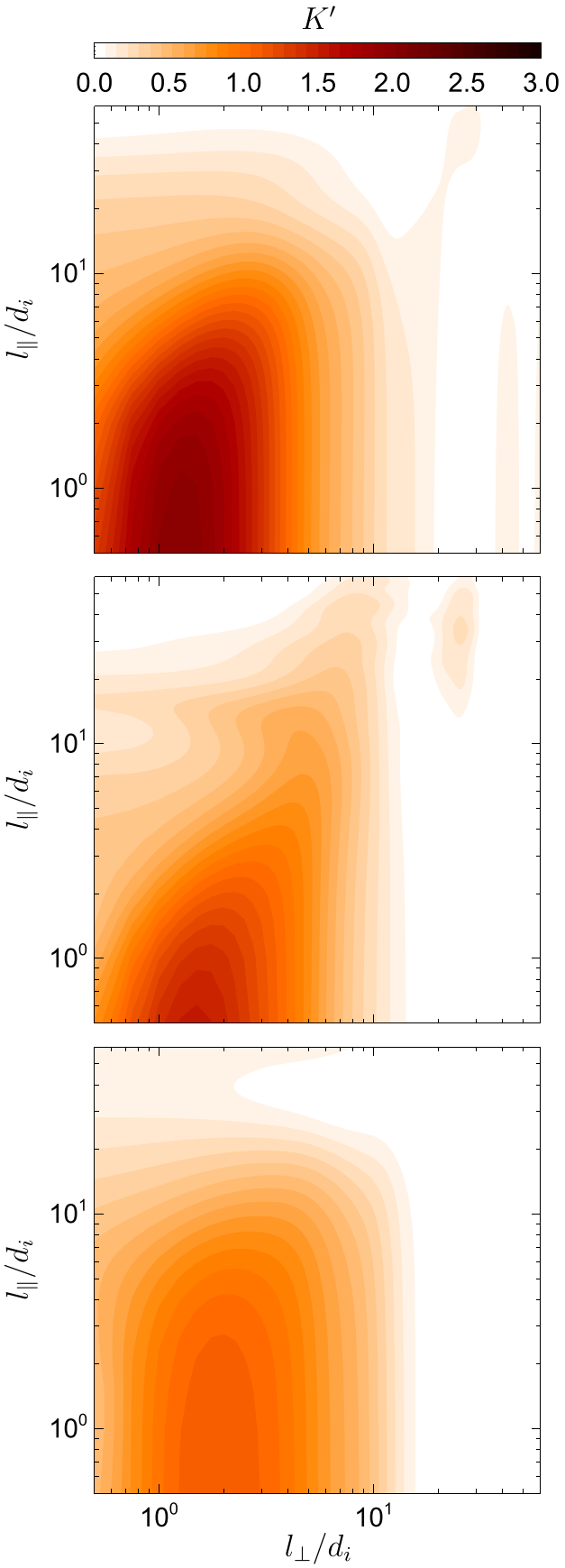


Figure 9. Color-scale plots of the excess kurtosis K' of the increment δB_y as functions of the separation $l_\perp$ and $l_\parallel$ for (top) $t = 0.10t_{\rm exp}$, (middle) $t = 0.14t_{\rm exp}$, and (bottom) $t = 0.20t_{\rm exp}$.

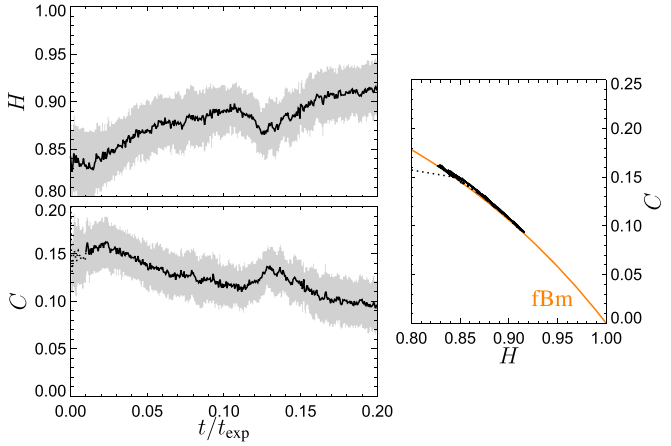


Figure 10. Evolution of (left top) the permutation entropy H and (left bottom) the statistical complexity C of the B_y component of the magnetic field calculated at about 45° with respect to the ambient magnetic field as functions of time (mean values shown in black, whereas the gray area denotes the mean values ± the standard deviation; the dotted lines denote an initial transition phase). (Right) Mean simulation data in the (H, C) plane (black line) compared to the prediction for the fractional Brownian motion (orange line); the dotted line denotes the initial transient phase.

given as

$$S(\boldsymbol{p}) = -\sum_{p_j \neq 0} p_j \ln p_j \tag{2}$$

and the permutation entropy H is normalized to its maximum value as

$$H(\boldsymbol{p}) = \frac{S(\boldsymbol{p})}{\ln n!}. \tag{3}$$

The Jensen–Shannon complexity is given by

$$C(\boldsymbol{p}) = Q(\boldsymbol{p})H(\boldsymbol{p}), \tag{4}$$

where

$$Q(\boldsymbol{p}) = -\frac{2S(\frac{\boldsymbol{p}+\boldsymbol{p}_e}{2}) - S(\boldsymbol{p}) - S(\boldsymbol{p}_e)}{\frac{n!+1}{n!}\ln(n!+1) - 2\ln(2n!) + \ln n!} \tag{5}$$

is a measure of the distance between $\boldsymbol{p}$ and $\boldsymbol{p}_e$, the probability vector for equally probable permutations, $\boldsymbol{p}_e = \{1/n!\}_{j=1,n!}$.

The two statistical quantities depend on many parameters (the scale, number of points, etc.) and are also affected by the noise level (Lamberti et al. 2004). Having a non-negligible noise level and a limited box size, we take 8×8 1D cuts (equidistantly separated) and calculate H and C for each cut every $5\omega_c i$ using four-point statistics ($n = 4$ in the definitions above). Figure 10 shows the evolution of the mean permutation entropy H and the mean statistical complexity C (and their standard deviations) of the B_y component of the magnetic field obtained for 1D cuts at the diagonal direction in the (x, z) plane (i.e., at about 45° as functions of time. The right panel of Figure 10 shows the evolution in the (H, C) plane of the mean values compared to the (four-point) prediction for the fractional Brownian motion series (Bandt & Shiha 2007; Zunino et al. 2008). Figure 10 (top) shows that as turbulence develops the permutation entropy H becomes about 0.88, whereas C reaches values around 0.13 and indicates a long-time trend of H to increase and C to decreases, as might be expected. However, when the fire-hose wave activity appears around $t = 0.14t_{\rm exp}$, H is temporarily reduced and C is enhanced;

these changes are significant in that they are somewhat larger than the corresponding standard deviations. The mean values of the permutation entropy H and the statistical complexity C are anti-correlated and (except for the initial phase when turbulence develops) H and C follow a path compatible with the prediction for the fractional Brownian motion (see Maggs & Morales 2013; Figure 10, right). We also calculated the permutation entropy and statistical complexity for 1D cuts parallel and perpendicular to the background magnetic field; calculations along these directions give similar results. However, in the perpendicular direction the variation of H and C due to the fire hose wave activity is rather weak.

We performed an additional simulation of a decaying (only 2D) turbulence with similar parameters but far from the unstable region using the expanding box model. In this simulation no fire hose wave activity is observed and the mean values of H and C (calculated on 1D spatial cuts along x of the B_y component) have the expected behavior: once the turbulent cascade is well-developed, H slowly increases, whereas C decreases (not shown here). We observe a similar evolution in a corresponding standard hybrid simulation. This supports the idea that the presence of quasi-coherent fire-hose wave activity leads to a decrease of the permutation entropy and an increase of the complexity.

4. Discussion and Conclusion

In this paper we used the 3D HEB simulation to investigate properties of the turbulent cascade and its relationship with fire-hose instabilities. We initialized the system with an isotropic spectrum of (relatively) large-scale Alfvénic fluctuations with zero cross-helicity. Nonlinear coupling of these modes leads to a turbulent cascade and energization of protons. Such energization is not, however, strong enough to compete with the anisotropic cooling due to the expansion, and protons develop an important parallel ($T_\perp < T_\parallel$) temperature anisotropy similar to in situ observations from the *Helios* spacecraft (Matteini et al. 2007); larger-amplitude turbulent fluctuations are needed to counter-balance the solar wind expansion (see Montagud-Camps et al. 2018). When the proton temperature anisotropy becomes strong enough, parallel and oblique fire hoses are destabilized and generate quasi-coherent wave packets with an amplitude much smaller than that of the background turbulence. The generated waves efficiently reduce the proton temperature anisotropy, they are partly reabsorbed by protons through cyclotron resonances, and then partly couple to and participate in the turbulent cascade. Turbulent fluctuations shape the plasma system, leading to the formation of a variable electromagnetic field as well as variable proton density, temperature anisotropy, agyrotropy, etc. The fire hose wave activity reduces the proton temperature anisotropy while it further increases the proton agyrotropy. Despite the inhomogeneity/nonuniformity and agyrotropy of the plasma system, the linear prediction based on the corresponding homogeneous and uniform gyrotropic approximation is in semi-quantitative agreement with the simulation results.

In the 2D HEB simulation of Hellinger et al. (2015) the expansion-driven fire hose fluctuations are by construction injected into the turbulent cascade; they are forced to have wave vectors perpendicular to the ambient magnetic field where the cascade proceeds. In this case, the simulation results indicate that the growth rate of unstable modes must be strong enough to compete with the cascade characterized by the nonlinear eddy turnover time $t_{\rm nl}$. In the real space, the fire-hose fluctuations were strongly localized in the 2D simulation between magnetic islands and tended to be aligned along the local most uniform direction. In the 3D simulation the fire-hose fluctuations appear to be outside the region dominated by the turbulent cascade; their wave vectors are quasi-parallel/oblique with respect to the ambient magnetic field and lie outside of the region in the wave-vector space ($k_\parallel$, $k_\perp$) dominated by the turbulent cascade. In this quasi-parallel/oblique region the nonlinear eddy turnover time ($t_{\rm nl} \propto 1/\delta B$) is long so that it does not present a large obstacle to the development of the instabilities. In the real space, the fluctuations have quasi-parallel/oblique propagation and are directed about along the ambient magnetic field (magnetic field lines) that also constitutes roughly the most uniform direction. We are inclined to speculate that the presence of the turbulent cascade has a tendency to push the unstable modes outside the region dominated by the cascade. More work is needed to test it.

The well-developed turbulence in the 3D simulation before the onset of the fire-hose instabilities exhibits anisotropic intermittency properties that correspond to the anisotropic cascade. The kurtosis depends strongly on the separation scale $l_\perp$ perpendicular to the ambient magnetic field (similar results are also obtained also for the standard 3D hybrid simulation of Franci et al. 2018b). The kurtosis saturates and decreases for scales $l_\perp \lesssim d_i$ and is weaker at the quasi-parallel direction $l_\parallel > l_\perp$. The reduction of the kurtosis is likely related to the (resistive) dissipation, and a relatively large resistivity is used to avoid the accumulation of the magnetic energy on small scales. The weak fire-hose wave activity affects the kurtosis and leads to its reduction at the quasi-parallel directions; the generated waves likely have a rather Gaussian character, which leads to a reduction of kurtosis; however, because of their weak amplitude, they do not significantly affect the statistical properties of fluctuations at oblique angles where the turbulent fluctuations dominate.

For the developed turbulence in the presented simulation before the onset of the fire-hose instabilities the Shannon entropy H and the Jensen–Shannon complexity C comparable to in situ observations in the solar wind (Weck et al. 2015; Weygand & Kivelson 2019), H increases and C increases with the time (corresponding to the radial distance) as expected (and observed in a simulation where the fire hose instabilities are not generated), and they follow the prediction for a fractional Brownian motion in the (H, C) plane, similar to the observational results of Weygand & Kivelson (2019). The fire-hose wave activity brings new information to the system and causes a decrease of the entropy H and an increase of the complexity C, as might be expected. Interestingly, even when the fire-hose waves are present, H and C keep following the prediction for a fractional Brownian motion. However, the meanings of H and C (and their connection to the fractional Brownian motion) are yet to be understood.

This wave activity is easily identified as a narrow peak on top of the background turbulence in 1D power spectra similar to observations, but only at quasi-parallel/oblique angles with respect to the ambient magnetic field. For more oblique angles, the fire-hose wave activity is not discernible because of its low amplitude compared to the turbulent background. We expect a similar behavior for in situ observations. In this case it may be possible to detect the wave activity based on the coherence property (Lion et al. 2016). Furthermore, as the instability-driven wave activity modifies the statistical properties of the turbulent fluctuations, one might ask if these quantities can be used to discern the generation of (quasi-coherent) wave activity (such as instability-driven waves) within a turbulent system. It seems that the intermittency/kurtosis is not very useful for that purpose, as it is only reduced in the

quasi-parallel direction. The Shannon entropy and the Jensen–Shannon complexity are more promising tools; in contrast to the kurtosis, they do not seem to be strongly dependent on the angles at which the time series are measured with respect to the ambient magnetic field. However, it is unclear whether they can be used for real observations, as the change of two quantities in the simulation is rather weak.

The present 3D simulation has many limitations. We used parameters similar to the 2D case of Hellinger et al. (2015), with an expansion about ten times faster than that in the solar wind. At the same time, the amplitude of the turbulent fluctuations were larger such that the ratio between the expansion and turbulence characteristic timescales is comparable to that observed in the solar wind. The fire hose-driven magnetic fluctuations reach a relatively low amplitude with respect to the ambient turbulence, but they are efficient for reducing the proton temperature anisotropy owing to the resonant character of their interaction with protons. For a realistic expansion time we expect an even weaker level of fluctuations (Matteini et al. 2006; Hellinger 2017); the realistic level of turbulent fluctuation is also lower, so we expect a similar relative amplitude of fire hose and turbulent fluctuations in the solar wind. A more important limitation of the present results is the size of the simulation box. Due to the limited resources we have a relatively small box size and we initially inject the energy at relatively small scales compared to the solar wind conditions. Consequently, the level of intermittency observed in the simulation is relatively weak. Its formation on small scales is also possibly reduced by noise due to the limited number of particles per cell.

Despite these limitations, our numerical results show that fire-hose instabilities coexist with plasma turbulence and generate temperature-anisotropy reducing modes that lie in the spectral space outside the region dominated by the turbulent cascade. We expect similar behavior for other ion kinetic instabilities driven by particle temperature anisotropies and/or differential streaming in the solar wind (as indicated by in situ observations of Klein et al. 2018), except possibly for the mirror instability that drives strongly oblique modes; 2D numerical simulations show that the mirror instability coexists with plasma turbulence (Hellinger et al. 2017). However, the present simulation results show that these 2D results are too limited and need to be revisited.

P.H. acknowledges grant 18-08861S of the Czech Science Foundation. L.F. was supported by the UK Science and Technology Facilities Council (STFC) grant ST/P000622/1. This work was supported by the Programme National PNST of CNRS/INSU co-funded by CNES. We thank T. S. Plachutta for useful comments and suggestions.

ORCID iDs

Petr Hellinger https://orcid.org/0000-0002-5608-0834
Lorenzo Matteini https://orcid.org/0000-0002-6276-7771
Simone Landi https://orcid.org/0000-0002-1322-8712
Luca Franci https://orcid.org/0000-0002-7419-0527
Andrea Verdini https://orcid.org/0000-0003-4380-4837
Emanuele Papini https://orcid.org/0000-0002-7969-7415

References

Alexandrova, O., Carbone, V., Veltri, P., & Sorriso-Valvo, L. 2008, ApJ, 674, 115
Alexandrova, O., Chen, C. H. K., Sorriso-Valvo, L., Horbury, T. S., & Bale, S. D. 2013, SSRv, 178, 101
Arzamasskiy, L., Kunz, M. W., Chandran, B. D. G., & Quataert, E. 2019, ApJ, 879, 53
Bandt, C., & Pompe, P. 2002, PhRvL, 88, 174102
Bandt, C., & Shiha, F. 2007, J. Time Ser. Anal., 28, 646
Bruno, R., & Carbone, V. 2013, LRSP, 10, 2
Cranmer, S. R., Matthaeus, W. H., Breech, B. A., & Kasper, J. C. 2009, ApJ, 702, 1604
Del Sarto, D., & Pegoraro, F. 2018, MNRAS, 475, 181
Dong, Y., Verdini, A., & Grappin, R. 2014, ApJ, 793, 118
Franci, L., Hellinger, P., Guarrasi, M., et al. 2018a, JPhCS, 1031, 012002
Franci, L., Landi, S., Matteini, L., Verdini, A., & Hellinger, P. 2015, ApJ, 812, 21
Franci, L., Landi, S., Verdini, A., Matteini, L., & Hellinger, P. 2018b, ApJ, 1, 26
Gary, S. P. 1993, Theory of Space Plasma Microinstabilities (New York: Cambridge Univ. Press)
Gary, S. P., Goldstein, B. E., & Steinberg, J. T. 2001, JGR, 106, 24955
Gary, S. P., Jian, L. K., Broiles, T. W., et al. 2016, JGRA, 121, 30
Gary, S. P., Li, H., O'Rourke, S., & Winske, D. 1998, JGR, 103, 14567
Grappin, R., Velli, M., & Mangeney, A. 1993, PhRvL, 70, 2190
Hellinger, P. 2017, JPlPh, 83, 705830105
Hellinger, P., Landi, S., Matteini, L., Verdini, A., & Franci, L. 2017, ApJ, 838, 158
Hellinger, P., & Matsumoto, H. 2000, JGR, 105, 10519
Hellinger, P., & Matsumoto, H. 2001, JGR, 106, 13215
Hellinger, P., Matteini, L., Landi, S., et al. 2015, ApJL, 811, L32
Hellinger, P., & Trávníček, P. 2005, JGRA, 110, A04210
Hellinger, P., & Trávníček, P. 2008, JGRA, 113, A10109
Hellinger, P., Trávníček, P., Kasper, J. C., & Lazarus, A. J. 2006, GeoRL, 33, L09101
Hellinger, P., Trávníček, P. M., Štverák, Š., Matteini, L., & Velli, M. 2013, JGRA, 118, 1351
Jian, L. K., Russell, C. T., Luhmann, J. G., et al. 2009, ApJL, 701, L105
Klein, K. G., Alterman, B. L., Stevens, M. L., Vech, D., & Kasper, J. C. 2018, PhRvL, 120, 205102
Klein, K. G., & Howes, G. G. 2015, PhPl, 22, 032903
Lamberti, P. W., Martin, M. T., Plastino, A., & Rosso, O. A. 2004, PhysA, 334, 119
Lion, S., Alexandrova, O., & Zaslavsky, A. 2016, ApJ, 824, 47
López-Ruiz, R., Mancini, H. L., & Calbet, X. 1995, PhLA, 209, 321
MacBride, B. T., Smith, C. W., & Forman, M. A. 2008, ApJ, 679, 1644
Maggs, J. E., & Morales, G. J. 2013, PPCF, 55, 085015
Markovskii, S. A., & Vasquez, B. J. 2011, ApJ, 739, 22
Maruca, B. A., Kasper, J. C., & Gary, S. P. 2012, ApJ, 748, 137
Matteini, L., Hellinger, P., Goldstein, B. E., et al. 2013, JGRA, 118, 2771
Matteini, L., Hellinger, P., Landi, S., Trávníček, P. M., & Velli, M. 2012, SSRv, 172, 373
Matteini, L., Landi, S., Hellinger, P., & Velli, M. 2006, JGRA, 111, A10101
Matteini, L., Landi, S., Hellinger, P., et al. 2007, GeoRL, 34, L20105
Matthaeus, W. H., & Velli, M. 2011, SSRv, 160, 145
Matthaeus, W. H., Wan, M., Servidio, S., et al. 2015, RSPTA, 373, 20140154
Matthews, A. 1994, JCoPh, 112, 102
Mininni, P. D., & Pouquet, A. 2009, PhRvE, 80, 025401
Montagud-Camps, V., Grappin, R., & Verdini, A. 2018, ApJ, 853, 153
Ofman, L. 2019, SoPh, 294, 51
Olivier, C. P., Engelbrecht, N. E., & Strauss, R. D. 2019, JGRA, 124, 4
Oughton, S., Priest, E. R., & Matthaeus, W. H. 1994, JFM, 280, 95
Papini, E., Franci, L., Landi, S., et al. 2019, ApJ, 870, 52
Parashar, T. N., Matthaeus, W. H., & Shay, M. A. 2018, ApJL, 864, L21
Parashar, T. N., Shay, M. A., Cassak, P. A., & Matthaeus, W. H. 2009, PhPl, 16, 032310
Petrosyan, A., Balogh, A., Goldstein, M. L., et al. 2010, SSRv, 156, 135
Scudder, J., & Daughton, W. 2008, JGRA, 113, A06222
Servidio, S., Valentini, F., Perrone, D., et al. 2015, JPlPh, 81, 325810107
Shebalin, J. V., Matthaeus, W. H., Montgomery, D., et al. 1983, JPlPh, 29, 525
Stansby, D., Perrone, D., Matteini, L., Horbury, T. S., & Salem, C. S. 2019, A&A, 623, L2
Štverák, Š., Trávníček, P. M., & Hellinger, P. 2015, JGRA, 120, 8177
Valentini, F., Servidio, S., Perrone, D., et al. 2014, PhPl, 21, 082307
Verdini, A., & Grappin, R. 2015, ApJL, 808, L34
Verdini, A., Grappin, R., Hellinger, P., Landi, S., & Müller, W. C. 2015, ApJ, 804, 119
Weck, P. J., Schaffner, D. A., Brown, M. R., & Wicks, R. T. 2015, PhRvE, 91, 23101
Weygand, J. M., & Kivelson, M. G. 2019, ApJ, 872, 59
Wicks, R. T., Alexander, R. L., Stevens, M., et al. 2016, ApJ, 819, 6
Wu, P., Wan, M., Matthaeus, W. H., Shay, M. A., & Swisdak, M. 2013, PhRvL, 111, 121105
Zunino, L., Pérez, D. G., Martín, M. T., et al. 2008, PhLA, 372, 4768